A Computational Model for Cavitation Using Volume-of-Fluid Method

M. Passandideh-Fard[1] and E. Roohi[2]

[1]*Assistant Professor (mpfard@um.ac.ir),* [2]*Graduate Student*
Department of Mechanical Engineering, Ferdowsi University of Mashhad, Mashhad, Iran

ABSTRACT

In this paper, unsteady 2D/axisymmetric simulations of cavitating flows are performed using a modified "Volume-of-Fluid" (VOF) method. Simulation of the cavitation is based on a homogenous equilibrium flow model. To predict the shape of the cavity, Navier-Stokes equations in addition to an advection equation for liquid volume fraction are solved. Mass transfer between the phases is treated as a sink term in VOF equation. The numerical method is used for different geometries in a wide range of cavitation numbers. Computed shapes of cavities were found to be in good agreement with those of the reported experiments. Simulation results also compared well with those obtained from analytical relations.

1. INTRODUCTION

When the pressure in a liquid flow falls below the corresponding vapor pressure, the liquid evaporates. This phenomenon, named cavitation, has many applications in the industry and is categorized by a dimensionless number: $\sigma = \frac{P_\infty - P_v}{0.5\rho V_\infty^2}$ called cavitation number where P_v is the vapor pressure, ρ the liquid density, and P_∞, V_∞ are the main flow pressure and velocity, respectively. When a liquid flows over a solid object, as the fluid velocity increases (or cavitation number decreases) five different cavitation regimes are observed in the flow behind the object: incipient- , shear- , cloud- , partial-, and super-cavitation. The steady cavitation regime that occurs at high flow velocities (or low cavitation numbers) is called supercavitation which is the main subject of this paper.

Using computational models for cavitation has been around for the last few decades. Early works mainly used potential flow theory. Complex characteristics of cavitating flows such as sharp changes in the fluid density, existence of a moving boundary and the requirement of modeling phase change prevented the development of computational algorithms based on Navier-Stokes equations. Following the advancement in CFD methods, cavitation models based on Navier-Stokes equations emerged in early 1990's. Among these models, the two main categories are interface tracking method and homogeneous equilibrium flow [1]. In the first category, a constant pressure (vapor pressure) is assumed for the cavity region (the so-called cavity) and a wake model is used to predict the shape of the cavity in adaptive grids. The current study is based on the second category where a single-fluid modeling approach is employed for both phases. Homogeneous equilibrium flow model assumes that there is no velocity slip between the phases at the cavity interface. Various models in this category differ in the relation that defines the variable density field. In one model, barotropic water-vapor state laws are used to calculate density. A more precise approach is to solve an advection equation for liquid (or vapor) volume fraction and compute density according to volume fraction of the two phases. This approach, so-named Transport Based Equation Model (TEM), has widely been applied to simulate cavitation. In this approach, the selection of an appropriate mass transfer model and an algorithm for advection equation are the main issues. Yuan et al. [2] suggested a cavitation model based on Rayleigh relation [1]. Singhal et al. [3], Merkle et al. [4] and Kunz et al. [5] have used different mass transfer models based on semi-analytical equations.

In order to precisely predict the cavity interface, VOF technique has increasingly been used to solve the advection equation. Frobenius and Schilling [6] and Wiesche [7] used this technique to simulate cavitation over hydrofoils and pump impellers. A review of the reported literature reveals that VOF method can accurately capture cavity shape and characteristics.

In this study, a modified VOF technique based on Youngs' PLIC algorithm [8] is combined with a mass transfer model of Kunz et al. [5] to simulate cavitation. The developed numerical model is applied to different geometries in a wide range of cavitation numbers and the results are compared with those of the reported experiments and analytical relations.

2. NUMERICAL METHOD

There are two main issues regarding the developed model: the advection of the cavity interface using VOF method, and the mass transfer model between the liquid and vapor phases. In this section, we present the two parts separately.

2.1 VOF Algorithm

The governing equations are:

$$\vec{\nabla}\cdot\vec{V}=0 \tag{1}$$

$$\frac{\partial\vec{V}}{\partial t}+\vec{\nabla}(\vec{V}\vec{V})=-\frac{1}{\rho}\vec{\nabla}p+\frac{1}{\rho}\vec{\nabla}\cdot\vec{\tau}+\frac{1}{\rho}\vec{F}_b \tag{2}$$

where $\vec{V}$ is the velocity vector, p is the pressure and F_b represents body forces acting on the fluid. The cavity interface is advected using VOF method by means of a scalar field f whose value is unity in the liquid phase and zero in the vapor. When a cell is partially filled with liquid, f will have a value between zero and one.

The discontinuity in f is propagating through the computational domain according to:

$$\frac{df}{dt}=\frac{\partial f}{\partial t}+\vec{V}\cdot\vec{\nabla}f=S \tag{3}$$

where S is the appropriate cavitation mass transfer sink term. Different cavitation models for evaluating S will be discussed in the next section. For the advection of volume fraction f based on Eq. 3, different methods have been developed such as SLIC, Hirt-Nichols [9] and Youngs' PLIC [8]. The reported literature on the simulation of cavitation reveals that Hirt-Nichols method has been used by many researchers. In this study, however, we used Youngs' method, which is a more accurate technique.

Assuming the initial distribution of f to be given, velocity and pressure are calculated in each time step by the following procedure. The f advection begins by defining an intermediate value of f,

$$\tilde{f}=f^n-\delta t\vec{\nabla}\cdot(\vec{V}f^n) \tag{4}$$

Then it is completed with a "divergence correction"

$$f^{n+1}=\tilde{f}+\delta t(\vec{\nabla}\cdot\vec{V})f^n+\delta t(S^n) \tag{5}$$

A single set of equations is solved for both phases, therefore, density and viscosity of the mixture are calculated according to:

$$\rho=f\rho_l+(1-f)\rho_v \qquad \mu=f\mu_l+(1-f)\mu_v \tag{6}$$

where subscripts l and v denote the liquid and vapor, respectively. New velocity field is calculated according to the two-step time projection method as follows. First, an intermediate velocity is obtained,

$$\frac{\tilde{\vec{V}}-\vec{V}^n}{\delta t}=-\vec{\nabla}\cdot(\vec{V}\vec{V})^n+\frac{1}{\rho^n}\vec{\nabla}\cdot\vec{\tau}^n+\vec{g}^n+\frac{1}{\rho^n}\vec{F}_b^{\,n} \tag{7}$$

The continuum surface force (CSF) method [10] is used to model surface tension as a body force (F_b) that acts only on interfacial cells. Pressure Poisson equation is then solved to obtain the pressure field,

$$\vec{\nabla}\cdot[\frac{1}{\rho^n}\vec{\nabla}p^{n+1}]=\frac{\vec{\nabla}\cdot\tilde{\vec{V}}}{\delta t} \tag{8}$$

Next, new time velocities are calculated by considering the pressure field implicitly,

$$\frac{\vec{V}^{n+1}-\tilde{\vec{V}}}{\delta t}=-\frac{1}{\rho^n}\vec{\nabla}p^{n+1} \tag{9}$$

2.2 Cavitation Models

Different cavitation mass transfer models have been suggested; they are mainly based on I) Rayleigh equation and II) semi-analytical models. In the current study, both categories were examined and an appropriate model was implemented in the advection equation (Eq. 3) as follows.

In the first category, a simplified Rayleigh equation is used as

$$\frac{3}{2}(\frac{dR}{dt})^2=\frac{P_v-P_l}{\rho_l} \tag{10}$$

where water vapor nuclei with a radius R is assumed to grow when the pressure drops below the vapor pressure, P_v. When applying this method for mass transfer across the cavity (the sink term in Eq. 3) we will have:

$$\frac{\partial f}{\partial t}+\vec{V}\cdot\vec{\nabla}f=-\frac{4\pi n_0R^2\dot{R}}{1+n_0\cdot\frac{4}{3}\pi R^3} \tag{11}$$

where n_0 is the initial vapor nucli. Rayleigh theroy was based on the balance of forces over spherical bubbles. It ignors bubble interactions, non-spherical buuble geometries and local mass-momentum transfer around the interface. It has been reported that these characteristics can become important in predicting cavity region, especially in the case of supercavitation [1]. Another drawback of this method is that it requires an estimation for the initial value of cavitation nuclei (n_0) and bubble radius (R). The amount of these values affect the predicted cavity length and diameter considerably [2].

The second category is based on semi-analytical models. These models are usually based on the modified Rayleigh theory or the conservation of mass-momentum around cavity interface [11]. The exact analytical relation for cavitation mass transfer

based on local mass-momentum conservation around cavity interface is [11, 12]

$$\frac{\partial f}{\partial t}+\vec{V}.\vec{\nabla}f=\frac{\rho_l Min(P_l-P_v,0)f}{\rho_v(V_{I,n}^{net})^2(\rho_l-\rho_v)t_\infty} + \frac{Max(P_l-P_v,0)(1-f)}{(V_{I,n}^{net})^2(\rho_l-\rho_v)t_\infty} \quad (12)$$

where $V_{I,n}^{net}$ is the net interface velocity relative to the local flow field and t_∞ is flow characteristic time defined as the ratio of solid body diameter to main flow velocity (D/V_∞). The two terms in the R.H.S of Eq. 12 are evaporation and condensation terms, respectively. The evaporation term reduces the amount of liquid (function f decreases) when pressure drops below the vapor pressure, while the condensation term will add to liquid (f increases) when the reverse occurs. The main drawback of this method is on approximating the value of $V_{I,n}^{net}$ for which some suggestions are reported in the literature [11, 12]. Merkle et al. [4] and Kunz et al. [5] proposed two semi-analytical models as follows. The Merkle's model reads

$$\frac{\partial f}{\partial t}+\vec{V}.\vec{\nabla}f=\frac{C_{dest}\rho_l Min(P_l-P_v,0)f}{\rho_v(0.5\rho_l V_\infty^2)t_\infty} + \frac{C_{prod}Max(P_l-P_v,0)(1-f)}{(0.5\rho_l V_\infty^2)t_\infty} \quad (13)$$

where C_{dest} and C_{prod} are weighting coefficients suggested as $C_{dest}=1.0$, $C_{prod}=80.0$ based on a numerical/experimental analysis. In the Kunz's model [5], the condensation term has a different form; this model suggests

$$\frac{\partial f}{\partial t}+\vec{V}.\vec{\nabla}f=\frac{C_{dest}\rho_v Min(P_l-P_v,0)f}{\rho_l(0.5\rho_l V_\infty^2)t_\infty} + \frac{C_{prod}(1-f)f^2}{\rho_l t_\infty} \quad (14)$$

where $C_{dest}=9\times10^5$, $C_{prod}=3.0\times10^4$. It can be seen that the difference between the evaporation term in Eq. 14 and in the other two models (Eqs. 12 and 13) is that in Kunz's model, the multiplying term (ρ_l/ρ_v) has been replaced by (ρ_v/ρ_l). As a result, coefficient C_{dest} in Kunz's model is relatively large to compensate for $(\rho_l/\rho_v)^2$ which has an order of about 10^6. The main difference between the three models (Eqs. 12-14) is in the condensation term which significantly affects the flow near the cavity closure region. Due to condensation, there will be a continuous flow of reentrant liquid jet near the cavity closure which in turn causes small vapor structures to detach from the end of the cavity continuously [13]. To include this phenomenon more effectively, Kunz's model assumes a moderate rate of constant condensation. According to Senocak and Shyy [11], Kunz's model reconstructs the cavity region more accurately than Merkle's model, especially in the closure region.

To select the appropriate model in this study, supercavitation behind a 240 mm diameter disk at a cavitation number of σ =0.2 was simulated using three different models of Rayleigh (Eq. 11 in a modified form to include vapor condensation), Merkle (Eq. 13) and Kunz (Eq. 14). Water properties were assumed to be: $\nu=10^{-6}$ m^2/s, ρ=1000 kg/m^3, and surface tension γ=0.072 N/m. And for vapor properties, we used: $\nu=24.18\times10^{-6}$ m^2/s and ρ=0.5542 kg/m^3. An analytical solution of the supercavitation behind a disk is available in the literature where the ratio of maximum length of the cavity to its maximum diameter is given by [13]

$$\frac{l_{cavity\,\max}}{d_{cavity\,\max}}=\frac{\sigma+0.008}{\sigma(1.7\sigma+0.066)} \quad (15)$$

This relation known as Richardt analytical relation gives a value of 6.81 for the disk cavitator under consideration.

Simulated supercavity regions using the three models are shown in Fig. 1. As seen in the figure, all three models predict a similar shape for the cavity. The Rayleigh model results in a value of length-to-diameter of around 7.42 which means that the model overestimates the shape of the supercavity by nearly 9% compared to the analytical solution. This is because the Rayleigh model is sensitive to the values of initial bubble radius and cavitation nuclei (R and n_0, respectively). Both semi-analytical models, however, predict the value of length-to-diameter ratio of around 6.95 which is in good agreement with the analytical value. In comparison between the two semi-analytical models, the Kunz model simulates cavity closure and vapor detachment more accurately than the Merkle's; as a result, all the simulations performed in this study were performed using the Kunz model of Eq. 14.

3. RESULTS AND DISCUSSION

In this section, first we provide the result of a mesh refinement study in which the grid size was progressively increased until the obtained simulation results were independent of size. This is done to justify the cell size we have used for the rest of simulations presented afterwards.

3.1 Grid Independency Analysis

In order to compare different mesh resolutions, a parameter called 'CPDR' is defined as the number of cells per disk radius. Supercavitaion behind a 38 mm diameter disk cavitator at a cavitation number of

σ =0.30 was simulated using three different cell sizes of 2.38, 1.58 and 1.27 mm corresponding to a resolution of 8, 12 and 15 CPDR, respectively. In Fig. 2, the results of numerical simulation for supercavity length, diameter and drag coefficient $C_D = Drag\ force/(0.5\rho V_\infty{}^2)$, are plotted versus mesh resolution parameter CPDR. The corresponding error of these parameters (when compared to Richardt analytical solution [13]) is shown in Fig. 3. The maximum error (12.8%) corresponds to the length of the supercavity for a CPDR of 8. The mesh refinement has a larger effect on C_D; the error in calculated C_D decreases to 1.4% for a CPDR of 15. Using a fine mesh also results in a more precise cavity closure reconstruction. Simulations performed in this paper, therefore, are based on a CPDR ranged from 12 to 15.

3.2 Model Validation

Case 1: Supercavitation behind a Disk Cavitator

The first test case considered is supercavitation behind a circular disk for which experimental and analytical results (such as Richardt relation, Eq. 15) are available in the literature [13]. For a cavitation number of σ =0.20 and a Reynolds number of Re=1.7×10^6, the evolution of supercavity formation is shown in Fig. 4. Cavitation starts inside two low pressure vortices formed in separated region behind the disk. With the development of supercavity region, pressure remains at a constant value of vapor pressure and does not drop any further. The steady supercavity shape forms at t=49 ms. The reentrant flow of water jet into the cavity at its closure region makes small bubble structures separate from supercavity (t=51 ms). Further downstream from the cavity closure, a stagnation point is formed which separates the main flow from reentrant jet. Due to an unsteady nature of reentrant jet, the position of stagnation point moves along the cavity centerline. The pressure coefficient at this point is far below 1.0 [13], in this case about 0.42.

Figure 5 compares the results of the model for this case with those of the experiments and analytical relations. The nondimensionalized supercavity's length vs. cavitation number is shown in this figure. The length of supercavity exponentially increases when σ decreases. Numerical results compares well with both experiments and theory. The small discrepancy between experimental results and those of the simulation (and theory) may be attributed to the effects of water tunnel walls on the experimental measurements. Figure 6 displays a comparison between simulations and analytical results for the characteristic parameter of disk cavitator, defined as $(\frac{L}{(D \times C_D^{0.5})})$; this parameter combines all aspects of a supercavity namely its length, diameter and drag coefficient in one number. As observed, the numerical results are in good agreement with those of the Richardt relation [13].

Case 2: Supercavitation behind a Cone Cavitator

In another test case, the supercavity behind a cone was considered. For a cavitation number of σ =0.20 and a Reynolds number of Re=1.87×10^6, pressure coefficient contours (C_p) are plotted in Fig. 7. As observed, C_p ranges from a minimum value of -0.20 inside the cavity to a maximum value of 1.0 at the cone head. Considering the definition of C_p and σ, it can be seen that the absolute value of pressure coefficient inside the cavity is equal to that of the cavitation number.

$$\begin{cases} 1)\ Cp = \dfrac{P - P_\infty}{0.5\rho V_\infty^2},\ P = P_v\ (in\ cavity) \\ 2)\ \sigma = \dfrac{P_\infty - P_v}{0.5\rho V_\infty^2} \end{cases} \Rightarrow Cp = -\sigma \qquad (16)$$

As a result, the constant contour of C_p= -0.20 is the supercavity boundary as well. Surface tension effects are important in the cavity closure region where a low pressure cavity gradually blends into the surrounding pressure.

A comparison between the results of the model for this case with experimental measurements and those of the analytical relations is presented in Fig. 8. It can be seen that the model accurately predicts the shape of the cavity. A close comparison between Figs. 5 and 8 reveals that the shape of supercavity behind a cone cavitator is smaller and thinner than that of a disk cavitator. This is because the separation region behind the cone, where the cavitation is formed, is smaller. It has been reported, however, that the ratio of $\frac{l_{cavity\,\max}}{d_{cavity\,\max}}$ is only a function of cavitation number and is independent of cavitator geometry as stated by Richardt relation (Eq. 15).

To investigate this statement using simulation results, a comparison was made between disk and cone cavitators at σ =0.20 as given in Table 1. It is seen that the model confirms the theory.

Cavitator shape	$\frac{l_{cavity\,\max}}{D_{cavitator}}$	$\frac{d_{cavity\,\max}}{D_{cavitator}}$	$\frac{l_{cavity\,\max}}{d_{cavity\,\max}}$
Cone	4.34	1.69	2.57
Disk	5.28	2.07	2.55

Table 1: Comparison of supercavity parameters for cone and disk cavitators.

3.3 Cloud and Partial Cavitation over a Cylinder

In this test case, cavitation over a blunt cylinder at two cavitation numbers of σ =0.30 and σ =0.20 was simulated; the results are shown in Figs. 9 and 10. Cavitation starts at vortices formed near the cylinder

wall and gradually grows. The simulations show that at a higher cavitation number (Fig. 9), the shape of the cavity exhibits a periodic behavior similar to that of the cloud cavitation where large vapor structures detaches from main cavity and the cavity grows again from the front edge of cylinder. At a lower cavitation number, a partial cavity with steady behavior is formed (Fig. 10). Experimental studies over Plano-circular hydrofoils show that cavity is thick and unsteady at high angles of attacks and high cavitation numbers, while it is steady and thin at low angles of attacks and low cavitation numbers [13]. At low cavitation numbers, the oscillation frequency of reentrant jet decreases, consequently, there is little chance for vapor shedding [13]. This behavior in cavitation around a cylinder can be justified by the same reason. Similar features over cylindrical bodies have been reported by Kunz et al. [5].

3.4 Cavity over a Cylinder with a Spherical Head

The cylinder geometry in this case is modified to include a semi-spherical head. The simulation results for σ =0.15 are shown in Fig. 11. Compared to the previous case, the cavity shape is thinner and smaller which could be explained by a smaller separation region in this case. A plot of velocity contours is shown in Fig. 12 where a core of reverse flow can be seen inside the cavity due to the vorticity there. Pressure coefficient contours around this geometry is shown in Fig. 13. The contour of C_p= -0.15 represents the cavity region and is in accordance with the interface shown in Fig. 11.

The pressure coefficient vs. cylinder length for different cavitation numbers is shown in Fig. 14. For a cavitation number of σ =0.20, the numerical results are compared with measurements where a good agreement is observed. For all cavitation numbers, C_p decreases from 1.0 at the stagnation point in front of the body to a constant value of ($-\sigma$) inside the cavity. Close to the cavity closure region, there is a large increase in pressure coefficient followed by a gradual reduction toward the main flow where the pressure coefficient is zero.

4. CONCLUSIONS

A numerical model has been developed that can accurately predict the cavitation that occurs behind a 2D/axisymmetric body in a liquid flow. The mass transfer between the liquid and vapor is modeled using Kunz's method [5] and the cavity interface is advected using a modified VOF technique based on Youngs' algorithm [8]. The developed model was used for different geometries in a wide range of cavitation numbers. Computed shapes of cavities and the drag force coefficient compared well with those of the reported experiments and analytical relations. The model accurately captured the cavity closure region with its transient features of reentrant jet movement and bubble detachment. In comparison with other available models for cavitation (e.g., the commercial software, Fluent) the developed algorithm is more efficient and needs far less CPU time and memory.

REFERENCES

1. G. Wang, I. Senocak, W. Shyy, T. Ikohagi, and S. Cao, *Progress in Aerospace Sciences*, Vol. 37, pp. 551-581, 2001.
2. W. Yuan, J. Sauer and G.H. Schnerr, *J. of Mechanical Ind.*, Vol. 2, pp. 383-394, 2001.
3. N. H. Singhal, A.K. Athavale, M. Li, and Y. Jiang, *J. of Fluids Engineering*, Vol. 124, pp. 1-8, 2002.
4. C.L. Merkle, J. Feng, and P.E.O. Buelow, in Proceedings of *the 3rd International Symposium on Cavitation, (CAV1998)*, Grenoble, France, 1998.
5. R.F. Kunz, D. A. Boger, D. R. Stinebring, T.S. Chyczewski, J.W. Lindau, and H. J. Gibeling, *Computers & Fluids*, Vol. 29, pp. 849-875, 2000.
6. M. Frobenius and R. Schilling, Cav03-GS-9-005, in Proceedings of *the 5th International Symposium on Cavitation*, Osaka, 2003.
7. S. Wiesche, *Heat Mass Transfer*, Vol. 41, pp. 615-624, 2005.
8. D.L. Youngs, *Num. Methods for Fluid Dynamics*, N.Y, 273-285, 1982.
9. F.H. Hirt and B.D. Nichols, *J. Comput. Phys.*, Vol. 39, p. 201, 1981.
10. J.U. Brackbill, D.B. Kothe and C. Zamach, *J. Comput. Phys.*, Vol. 100, pp. 335-354, 1992.
11. I. Senocak and W. Shyy, Proceeding of FEDSM 02, *ASME Fluid Engineering Division Summer Meeting*, Montreal, Canada, 2002.
12. J. Wu, G. Wang, and W. Shyy, *Int. J. Numer. Meth. Fluids*, Vol. 49, pp. 739-761, 2005.
13. J.P. Franc and J.M. Michel. *Fundamentals of Cavitation*, Section: 6. Kluwer Academic Publisher, Netherlands, 2004.R.E.

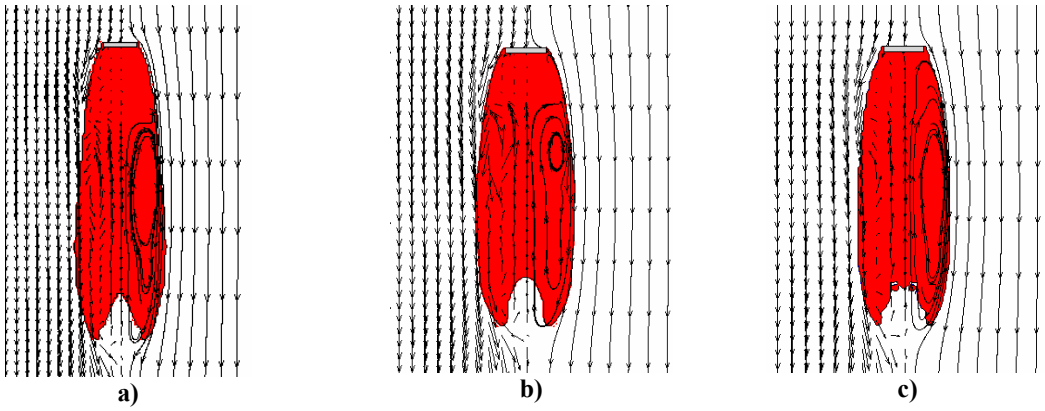

Figure 1: Comparison between three mass transfer models when used in simulating cavitation behind a 240 mm disk in a 31.20 m/s water flow with a cavitation number of σ =0.20: **a)** Rayleigh Model, Eq. 11 with n_0=2×10^{13}; **b)** Merkle Model, Eq. 13; and **c)** Kunz Model, Eq. 14.

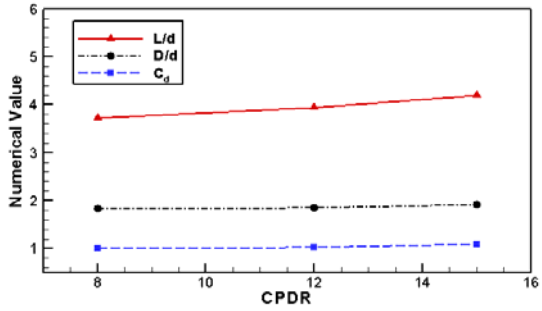

Figure 2: Numerical value of supercavity length, diameter and drag coefficient for three different mesh sizes.

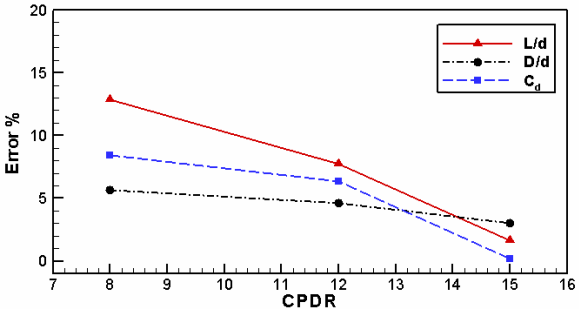

Figure 3: Corresponding error associated with three different mesh sizes of Fig. 2 when compared to Richardt analytical solution [13].

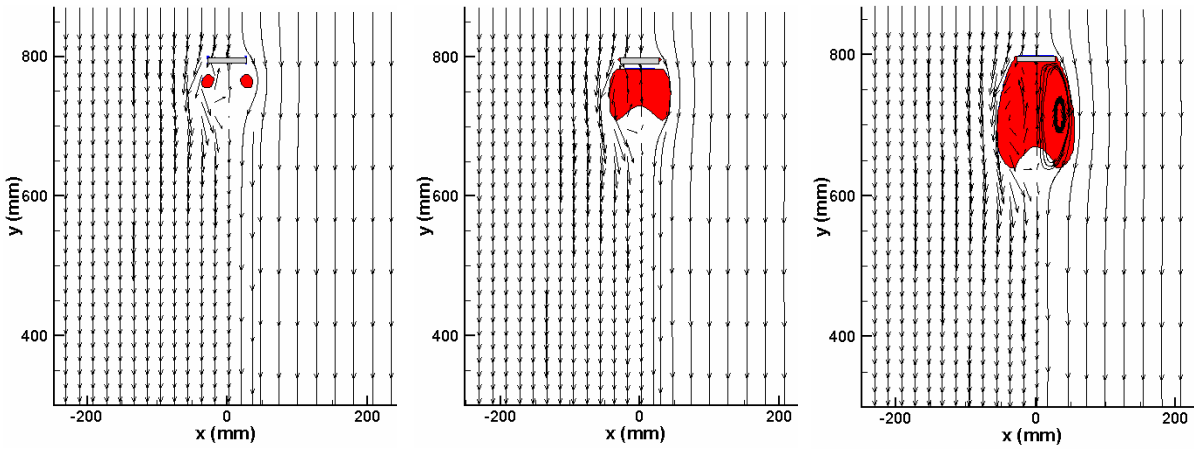

Figure 4: Evolution of supercavity formation behind a disk cavitator (σ =0.20, Re=1.7×10^6, d_{disk}=54 mm).

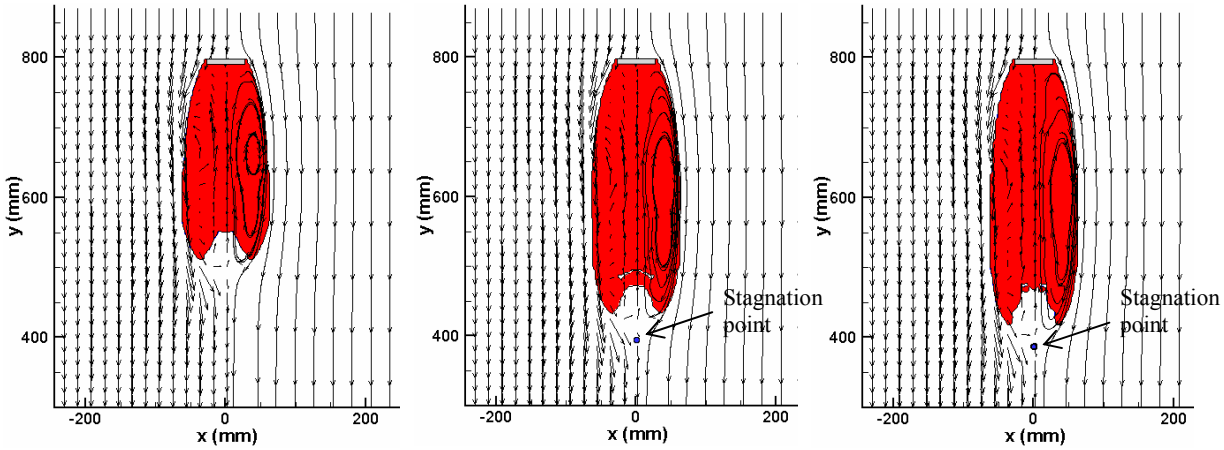

Figure 4: Continued.

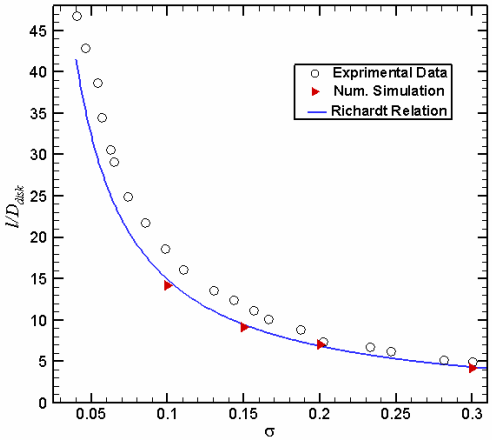

Figure 5: Supercavity length vs. cavitation number for a disk cavitator.

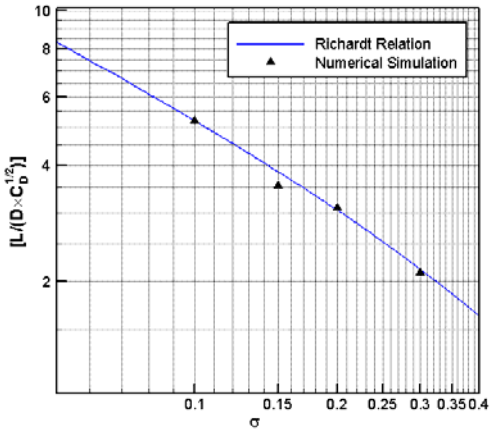

Figure 6: Cavitator characteristic parameter vs. cavitation number for a disk.

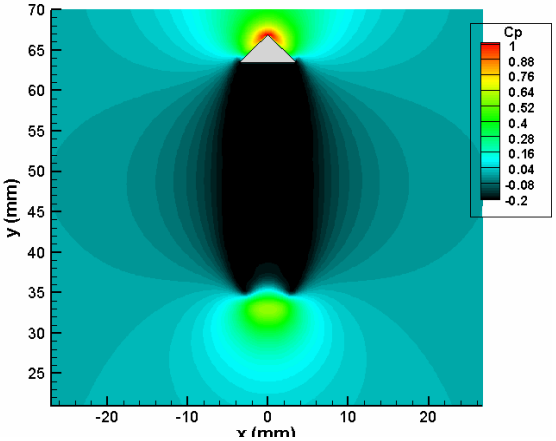

Figure 7: Pressure coefficient Contours around a cone cavitator (σ =0.20, Re=1.87×10^5, d_{cone}=7.34mm, Cone angle=90°).

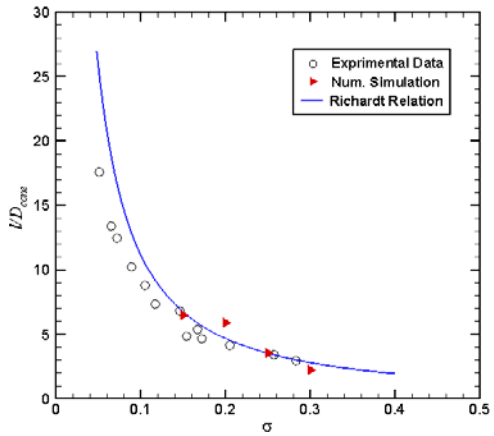

Figure 8: Supercavity length vs. cavitation number for a cone cavitator.

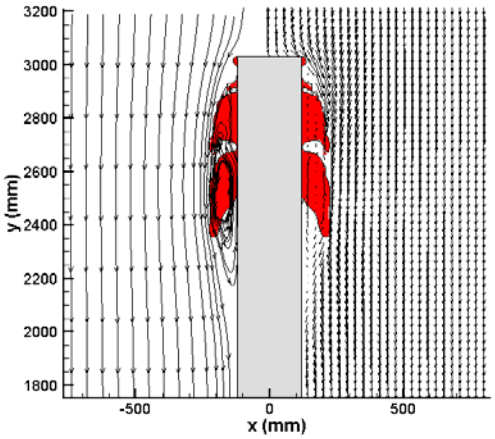

Figure 9: Cloud cavitation over a cylinder, (σ =0.30, d = 240 mm, Re=6.12×10^6).

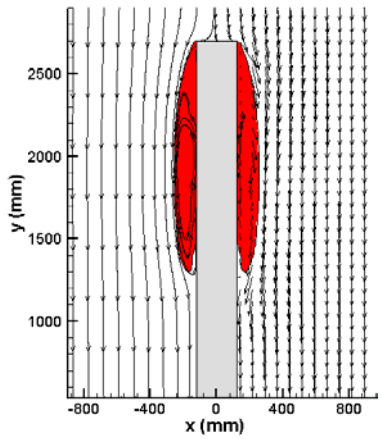

Figure 10: Partial cavitation over a cylinder, (σ =0.20, d = 240 mm, Re=7.50×10^6).

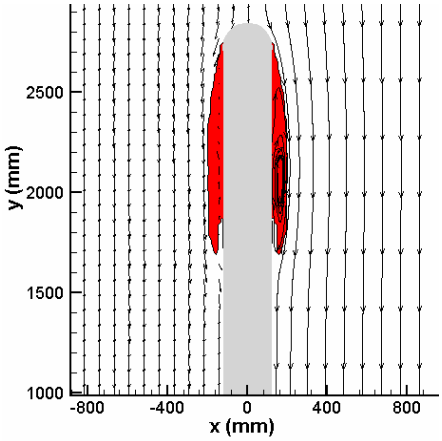

Figure 11: Partial cavitation over a cylinder with a spherical head, (σ =0.15, d = 240 mm, Re=8.65×10^6).

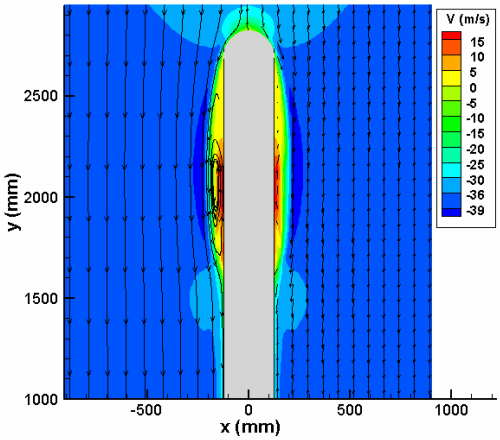

Figure 12: Velocity contours around a cylinder with a spherical head, (σ =0.15, d = 240 mm, Re=8.65×10^6).

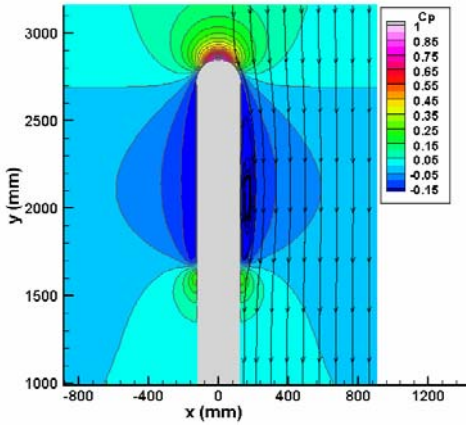

Figure 13: Pressure coefficient Contours around a cylinder with a spherical head, (σ =0.15, d = 240 mm, Re=8.65×10^6).

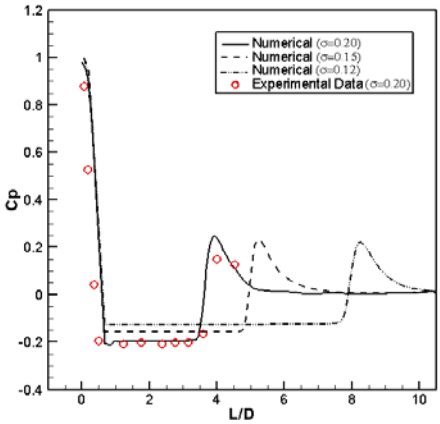

Figure 14: Pressure coefficient vs. non-dimensionalzed length for a cylinder with a spherical head.